Cement and Concrete Research 42 (2012) 903–918

Contents lists available at SciVerse ScienceDirect

Cement and Concrete Research

journal homepage: http://ees.elsevier.com/CEMCON/default.asp

Modelling early age hydration kinetics of alite

Aditya Kumar [a,*], Shashank Bishnoi [b], Karen L. Scrivener [a]

[a] Laboratory of Construction Materials, Ecole Polytechnique Fédérale de Lausanne, EPFL-STI-IMX-LMC, Station 12, 1015 Lausanne, Switzerland
[b] Department of Civil Engineering, Indian Institute of Technology Delhi, Hauz Khas, New Delhi 110016, India

ARTICLE INFO

Article history:
Received 12 December 2011
Accepted 13 March 2012

Keywords:
Modeling (E)
Dissolution
Nucleation and growth

ABSTRACT

The modelling platform μic [1] has been used to investigate the mechanisms occurring during the hydration of alite. It is shown that it is possible to obtain a good simulation of the hydration kinetics through the implementation of two mechanisms: a dissolution mechanism combined with nucleation and growth of products. The dissolution rate is varied according to the ratio β, between the ion activity product and the equilibrium solubility product according the theory published by Juilland et al. [2]. The solution concentrations are computed directly from the amount of alite dissolved taking into account the amount of water present and the amount of products formed, with activities and complex ion formation calculated according to standard methods. Saturation index calculations are implemented to compute the time of precipitation of C–S–H and portlandite (CH) individually. For the main heat evolution peak, the rate controlling mechanism switches to a modified form of boundary nucleation and growth. C–S–H grows in a diffuse manner in which the density of packing of the C–S–H phase increases with hydration [3]. The rate of heat evolution obtained from the simulations is compared with isothermal calorimetry data and good agreement is found.

1. Introduction

Alite (impure C_3S) constitutes about 50–80% of Portland cement and its hydration makes the major contribution towards the evolution of properties. This is especially true during the first day or so when alite hydrates rapidly forming portlandite (CH) and C–S–H (calcium–silicate–hydrates). The overall progress of the alite hydration is generally followed by monitoring the rate of heat evolution as obtained by Isothermal Calorimetry. Fig. 1 shows a typical heat evolution curve for the first 30 h. Five main stages can be identified:

1. Dissolution period: During the first minutes, alite dissolves and ions are released into the pore solution, but the reaction rapidly slows to a low rate.
2. Induction period: During the following hours low activity and low heat evolution are observed.
3. Acceleration period: The rate of heat evolution increases for several hours until it reaches a peak.
4. Deceleration period: The rate of heat evolution decreases for a few hours.
5. Slow hydration period: After the deceleration period, the hydration rate continues at a low decreasing level.

The mechanisms governing these periods have recently been reviewed by Bullard et al. [4]. Most controversy surrounds the first two periods. The two principal theories are that the slowdown in the rate of reaction occurs either: due to formation of a metastable barrier product on the surface of the reacting alite grains; or due to a decreasing rate of alite dissolution caused by the build-up in concentration of ions in solutions. Arguments for and against these hypothesis are fully discussed in [4].

In a recent publication [2] the similarities were demonstrated between alite reaction and the dissolution of many other mineral studied in geochemistry, where the theory of a slow dissolution step due to the buildup of ions in solution is widely accepted. The dissolution rate of most natural minerals does not follow a smooth relationship with respect to the saturation state of the solution [5,6]. Far from equilibrium, high rates of dissolution are enabled by etch pit opening. Whereas at high concentrations, the transition to the slow dissolution regime occurs at the levels of undersaturation still several orders of magnitude more dilute than the equilibrium concentration. In this regime, the driving force from undersaturation is insufficient to activate the etch pit opening and dissolution occurs by a retreating step mechanism that is much slower. We refer hereafter to this mechanism as *solution controlled dissolution*—SCD.

Periods 3 and 4 are now generally accepted to be controlled by the nucleation and growth of the main hydrate phase C–S–H. The kinetics in this period has been successfully reproduced by an analytical Boundary Nucleation and Growth algorithm [7] and numerically in the μic modelling platform [3]. In the later case it was found that period 4 was only well captured across a range of particle sizes, when C–S–H was presumed to grow out rapidly with a low packing density until the products growing from adjacent grains impinged. Concurrently

* Corresponding author.
E-mail address: a.kumar@epfl.ch (A. Kumar).

0008-8846/$ – see front matter © 2012 Elsevier Ltd. All rights reserved.
doi:10.1016/j.cemconres.2012.03.003

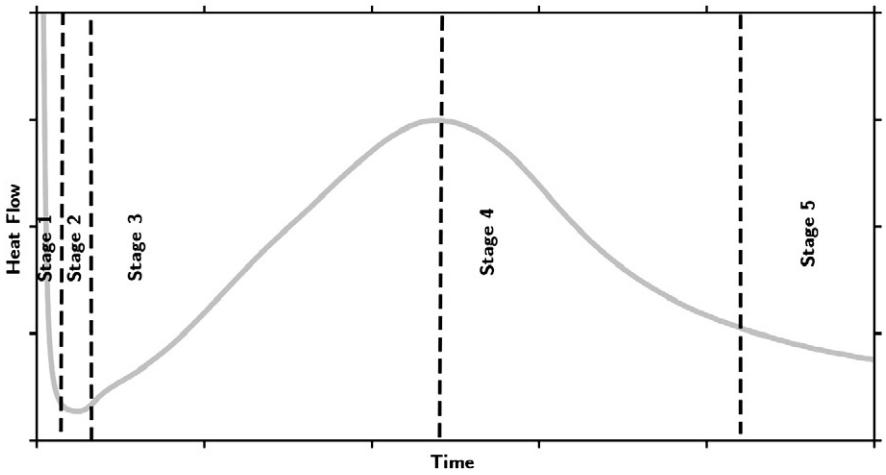

Fig. 1. Typical heat evolution curve of alite-model system until approximately 1 day of hydration.

this diffuse product densifies as a function of its distance from the underlying grain. This mechanism is subsequently referred to as *nucleation and densifying growth*—NDG.

As discussed in Refs. [4,7,8] and demonstrated in [3], the weight of evidence indicates that diffusion through the C–S–H layer is NOT the rate controlling mechanism in period 4, although it may become so during period 5.

Several numerical models [3,7,9–14] have been developed to describe and quantify the hydration of alite. These are discussed in a recent detailed review [4]. The modelling platform μic is unique in being able to rapidly simulate the microstructure: using a representative volume of around 100 μm in dimension; taking account of particles down to below 0.1 μm (around 2–10 million particles in the simulation); based on physical and chemical reaction mechanisms. Other models, either simplify simulation by dealing with a single particle [10]; have a resolution limited by the pixel size of around 1 μm [11]; implement kinetics purely by external empirical calibration with overall reaction rates measured by experiment [7,10,13]; require intensive computational power and protracted time-lengths to simulate digital microstructure and reaction rates [12].

In this paper we show how the two reaction mechanisms—solution controlled dissolution (SCD) for stages 1 and 2 and nucleation and densifying growth (NDG) for stages 3 and 4—can be used to capture the reaction kinetics for alite. During the SCD regime the composition of the solution phase is calculated at each step of the hydration process and thermodynamic calculations are used to determine when the different phases precipitate, this regime ends with the precipitation of portlandite which corresponds well with the onset of the acceleration period. In this regime the same parameters capture the whole range of particle sizes. The main heat evolution peak is well captured by the nucleation and densifying growth mechanism as first shown by Bishnoi and Scrivener [3]. There is a transition period between the two numerical regimes the reasons for which are discussed.

2. Simulation techniques

2.1. Basics of μic

The modelling platform μic [1] is used in this study. This is a microstructural modelling framework, which uses a vector approach to generate a resolution free microstructure. That is to say particles are represented geometrically as spheres with their respective positions and radii stored as *vectors*. Reactions and mechanisms are implemented as "plugins", which are user definable. Reactions, consumption of reactants and formation of products are carried out whilst monitoring the volumetric quantities of each phase. The model is flexible and can be used to study the effects of various processes and mechanisms in hydration of cement-based systems.

Particle size distribution plays an important role in determining the rate of reaction [3,15–17]. Finer particles with higher specific surface area react rapidly compared to cement with coarser particles having low specific surface area. In order to capture the effect of particle size distribution it is crucial to have a representation of the real particle size gradation in the model.

Initially, alite particles are randomly dispersed in the microstructure without any overlaps. Spheres are used to represent the alite particles using the real PSD as obtained from laser granulometry. Product phases which form as a result of hydration and their arrangement in the microstructure are also defined by the user. As the microstructure evolves with the growth of products, the effects of impingements between hydration products are taken into account to evaluate the overall rate of reaction.

In all the simulations presented here, the arrangement of hydrates is as shown in Fig. 2(a). Inner product C–S–H forms in the space left by the dissolving alite grains was assumed to have a uniform density of 2.10 gm/cm^3.[1] The density values used for alite, water and portlandite are 3.15 g/cm^3, 1.0 g/ml and 2.24 g/cm^3 respectively. Outer C–S–H forms as a layer initially with low packing density. This packing density increases over time from a low value to 2.10 g/cm^3, as described below and in Ref. [3]. It should be noted that the change in density of the outer C–S–H only indicates its packing density. As such, the OH/Si and Ca/Si ratios of outer C–S–H are the same as for inner C–S–H. Portlandite nucleates in the original water filled space. This arrangement of hydrates in the microstructure follows the widely accepted view of microstructural development from microscopical observations [18–21].

$$1.0.\,V_{C_3S} + 1.318.V_{H_2O} = 1.0.V_{inner\ C-S-H} + 0.495.V_{outer\ C-S-H} + 0.593.V_{CH} \quad (1)$$

Up until the precipitation of portlandite (stages 1 and 2, Fig. 1), the rate controlling mechanism is the *solution controlled dissolution* (SCD) of alite. The rate of dissolution is determined by the solution concentration following the hypothesis advances by Juilland et al. [2], as described below. Subsequently the main heat evolution peak is fit by a mechanism of nucleation and densifying growth (NDG). There is a virtual starting point for the NDG regime at t_0. The transition

[1] We are aware of the extensive debate about the density of C–S–H, which depends on the water content. We consider the value of 2.1 for inner or "high density" C–S–H to be reasonable for a composition of C1.7SH4 as expected in standard systems. However changes in this value will only have a minor impact on the rest of the paper.

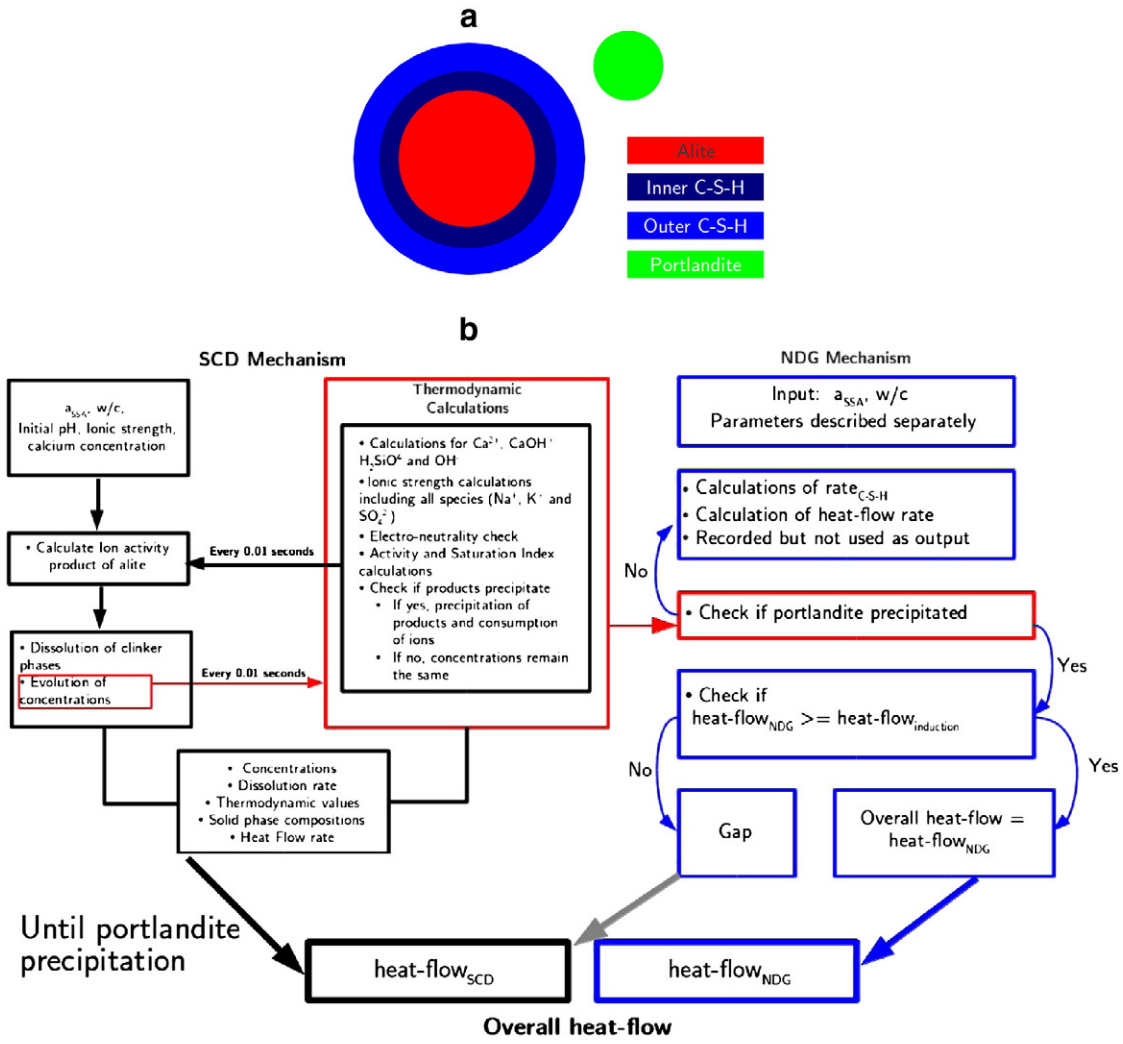

Fig. 2. (a) Distribution of phases in different cementitious systems, as used in the model (b) Flow chart depicting the mechanisms and their order of implementations in the simulations.

between the two regimes is discussed later. The main steps in the simulation process are shown in Fig. 2(b).

As alite dissolves and hydrates, C–S–H (inner and outer products) and portlandite (CH) are formed according to volumes given in Eq. (1), where the H/S ratio assumed for C–S–H is 4.0. The heat released under isothermal conditions is computed by using the standard enthalpy of reactions [20,21], as given in Table 1. At each step, the amount of each hydrated alite is calculated and used to compute the heat that would be released under isothermal conditions at T= 293.15 K. The cumulative heat released is then computed by the addition of heat released in individual steps. The rate of heat evolution is computed by differentiating the rate of cumulative heat released with time.

The heat evolution during the SCD phase is computed using the set of Eqs. (2)–(4).

$$Q_1 = -\frac{dm_{alite}}{dt}.H_{alite\ dissolution} \quad \text{(before C—S—H precipitates)} \tag{2}$$

Table 1
Standard enthalpies for alite reactions.

Reaction	Heat released (kJ/mol)
C_3S dissolution	−120 [20,21]
C–S–H precipitation	30 [20,21]
Portlandite precipitation	20 [20,21]

$$Q_2 = -\frac{dm_{alite}}{dt}.H_{alite\ dissolution} + m_{C-S-H}\,(dt).H_{C-S-H\ formation} \quad \text{(after C—S—H precipitates)} \tag{3}$$

$$Q_3 = Q_2 + m_{CH}\,(dt).H_{CH\ formation} \quad \text{(after C—S—H and CH precipitate)} \tag{4}$$

where, Q, H and m are the heat flow rate, enthalpy and mass respectively. The values for the enthalpy of alite dissolution and C–S–H and CH precipitation are shown in Table 1.

The heat evolution during the NDG regime is calculated using Eq. (5).

$$Q_{NDG} = -\frac{dm_{alite}}{dt}.H_{alite\ hydration} \tag{5}$$

where, $H_{alite\ hydration}$ is fixed at as 484 J/g.

2.2. Solution controlled dissolution

The dissolution of alite plays a key role in the evolution of the concentration of ions in the pore solution. It has been shown by Bullard et al. [22] that the concentration in solution reaches equilibrium very fast throughout the simulation volume. Furthermore, any concentration

gradients only exist on the scale of the distances between particles, which are very small (a few μm). Therefore, the solution concentrations are considered to be uniform throughout the simulation volume.

The dissolution of alite is described by Eq. (6). In this study "[]" and "{}" represent concentrations and activities respectively.

$$C_3S + 3H_2O \rightarrow 3Ca^{2+}_{(aq)} + 4OH^{-}_{(aq)} + H_2SiO_4^{2-}{}_{(aq)} \quad (6)$$

Juilland et al. [2] proposed that the rate of dissolution of alite varies as a function of the undersaturation of alite. At high degrees of undersaturation, i.e. on, and shortly after the addition of water, the dissolution is rapid, with the creation of etch pits. As ions enter solution, the undersaturation of the solution decreases until a critical degree of undersaturation is reached, where there is no longer enough energy to generate etch pits and the rate of dissolution slows down dramatically. Beyond this point dissolution is slow corresponding to dissolution by step retreat from existing etch pits. The dependence of dissolution rate on undersaturation close to this transition is controversial as some claim it is almost a step change [23], but here we assume that the rate of dissolution varies linearly with the parameter β_{alite}, which is the ion activity product of the ions in solution divided by the equilibrium solubility products (Eq. (7)), as this fits best with data report in the literature [24–26]. While β_{alite} represents the degree of undersaturation, log β_{alite} is the Saturation Index (SI_{alite}).

$$\beta_{alite}(t) = \frac{IAP_{alite}(t)}{K_{sp\ alite}} \quad (7)$$

where, $IAP_{alite}(t) = \left\{Ca^{2+}\right\}^{3.0}.\{OH^-\}^{4.0}.\left\{H_2SiO_4{}^{2-}\right\}^{1.0}$ is the ion activity product for alite and, $K_{sp\ alite} = 1.14.\ 10^{-4.0}$ is the equilibrium solubility product for alite.

The value for the solubility product of alite is a matter of discussion; here we use the value given by Bellmann et al. [24], which takes $H_2SiO_4^{2-}$ as the primary charged silicate species in solution. It should be noted that the value of both Ion Activity Product and Solubility product of alite will change depending on the choice of primary charged silicate species.

Overall the rate of dissolution of alite (μmol m^{-2} s^{-1}) is described mathematically by Eqs. (8a) and (8b). This equation was modified from the form as originally described by Damidot et al. [25] in the light of hypotheses advanced by Juilland et al. [2], a brief description of which is provided above. It describes the dissolution regimes of fast dissolution facilitated by etch pit formation for undersaturation below the critical value of β_{max} (for $\beta_{alite} \leq \beta_{max}$ given by Eq. (8a)) and slow dissolution driven by step retreats beyond the critical undersaturation (for $\beta_{alite} > \beta_{max}$ given by Eq. (8b)). The negative sign in the equations indicates loss in the mass of alite as a function of time as dissolution progresses.

$$\frac{dm_{alite}(t)}{dt} = [-k_{diss}\ .a_{SSA.}\ (\beta_{max} - \beta_{alite}(t))] - a_{SSA.}c_{step\ retreat} \quad (8a)$$

for $\beta_{alite}(t) \leq \beta_{max}$, and

$$\frac{dm_{alite}(t)}{dt} = -a_{SSA.}c_{step\ retreat} \quad (8b)$$

for $\beta_{alite}(t) > \beta_{max}$

In Eqs. (8a) and (8b), dm is the amount of alite dissolved, β_{max} is the critical degree of undersaturation of alite, k_{diss} (μmol kg m^{-4} s^{-1}) is a dissolution rate constant, a_{SSA} (m^2 kg^{-1}) is the specific surface area of particles divided by the volume fraction of the water in the representative volume, and $c_{step\ retreat}$ (μmol kg m^{-4} s^{-1}) is the step retreat constant. In the simulations, $\beta_{alite}(t)$ is calculated at each step based on the amount of alite dissolved and taking into account the total volume of water present in the representative volume. The rate of dissolution of alite varies as a linear function of undersaturation (β) when the undersaturation is high. When the undersaturation approaches a critical undersaturation value, given by β_{max}, dissolution continues at a constant value driven by step retreats (given by a_{SSA}. $c_{step\ retreat}$). The equation consists of three parameters which need to be calibrated: k_{diss}, β_{max} and $c_{step\ retreat}$. The calibrations of these parameters are discussed in Section 2.6.

With the dissolution equation implemented in the present form, the effects of surface area of alite particles can be described without the need for any modification in the format of the equation. As the evolution of IAP of alite is also implemented in the model, the effects of initial pore solution states can also be described. The description of the effects of these parameters is further discussed in Sections 3 and 5.

2.3. Activity calculations

Solubility calculations were implemented to compute the time of precipitation of C–S–H and portlandite in the model. The molality of all species in the model were calculated using the concentration of ionic species as obtained from simulation of dissolution of alite and taking into account the volume of water present in the representative volume.[2] Eq. (9) describes the activity of species in a solution. The expression for calculating the ionic strength is given by Eq. (10).

$$a_i = m_i.\gamma_i \quad (9)$$

$$I = 0.5.\sum m_i.z_i^2 \quad (10)$$

Where γ_i is the activity coefficient, z_i is the unit charge and m_i (mol kg^{-1}) is the molality of the species i. For the calculations of the activity coefficients, Truesdell–Jones form of [28] extended Debye–Hückel equation shown by Eq. (11) was used. This equation is applicable for electrolytes having an ionic strength up to 2.0 mol/L, which is accepted as a good upper-bound for cement-based systems.

$$\log \gamma_i = \frac{-A_T Z_i^2 \sqrt{I}}{1 + B_T a_i \sqrt{I}} + b_i \cdot I \quad (11)$$

where,

$$A_T = \left(2.74 \cdot 10^{-6}\right)T^2 + \left(-7.60 \cdot 10^{-4}\right)T^1 + (0.4916) \quad (12a)$$

$$B_T = \left(1.62.10^{-4}\right)T^1 + (0.2799) \quad (12b)$$

T (K) is the temperature, I (mol kg^{-1}) is the ionic strength and, a_i (Å) and b_i (Å) are Kielland ion-specific parameters. Values of A_T and B_T were calculated by using a temperature value of 293.15 K in Eqs. (12a)–(12b). The values of a_i and b_i for different ionic species used in the simulations are shown in Table 2.

The expression of Saturation Index (SI) for any phase in solution is given by Eq. (13)

$$SI = \log\left(\frac{IAP}{K_{sp}}\right) \quad (13)$$

where IAP is the ion activity product and K_{sp} is the solubility product. A negative value of SI implies undersaturation, a positive value indicates supersaturation and SI = 0 implies equilibrium with respect to the pore solution. A product is expected to precipitate when it is supersaturated with respect to the pore solution.

[2] Molality (m_i) = moles of species i (in moles)/Mass of water (in kg). Water is assumed to have a density of 1 g/ml here.

Table 2
Ion specific parameters for ionic species. All values have been adapted from [28].

Ionic Species	a_i (A)	b_i (A)
Ca^{2+}	4.86	0.15
OH^-	10.65	0.21
[a] $H_2SiO_4^{2-}$	$1/B_T$	$0.30/A_T$

[a] For $H_2SiO_4^{2-}$, Davies form of equation was used. The ion-specific parameters were modified to incorporate the effect of temperature.

2.4. C–S–H precipitation

There is no widely accepted form of the IAP for C–S–H. Rothstein et al. in their study [29], reported Eq. (14a) to describe the solubility of C–S–H. This equation assumes a fixed Ca/Si ratio of 1.7 and does not consider contributions of ions such as $CaOH^+$. Glasser [30] proposed Eq. (14b), which assumes a Ca/Si ratio of 1.75 and takes into account the contributions of $CaOH^+$. In this equation, y represents the ratio of concentration of $CaOH^+$ ions in the solution to the sum of the Ca^{2+} and $CaOH^+$ concentration. At the high pHs occurring in hydration the formation of $CaOH^+$ is important and cannot be ignored (Fig. 3), therefore we used a generalized form of Eq. (14b); rewritten as Eq. (15) to account for variability of the Ca/Si ratio.

$$IAP_{CSH-Rothstein} = \left\{Ca^{2+}\right\}^{1.70}.\{OH^-\}^{1.40}.\left\{H_2SiO_4^{2-}\right\}^{1.0} \quad (14a)$$

$$IAP_{CSH-Glasser} = \left\{Ca^{2+}\right\}^{\left(1.75-\frac{y}{2}\right)}.\{OH^-\}^{\left(1.5-\frac{y}{2}\right)}.\left\{H_2SiO_4^{2-}\right\}^{1.0}.\left\{CaOH^+\right\}^{\left(\frac{y}{2}\right)} \quad (14b)$$

$$IAP_{CSH} = \left\{Ca^{2+}\right\}^{\left(\frac{Ca}{Si}-\frac{y}{2}\right)}.\{OH^-\}^{\left(2\cdot\frac{Ca}{Si}-\frac{y}{2}-2.0\right)}.\left\{H_2SiO_4^{2-}\right\}^{1.0}.\left\{CaOH^+\right\}^{\left(\frac{y}{2}\right)} \quad (15)$$

To calculate the activity of the $CaOH^+$ species, the law of mass-action was used (Eq. (16), [31,32]). Using this equation, the concentration of $CaOH^+$ can be computed using the set of equations described by Eqs. (16)–(18), where γ_{Ca2+} and γ_{CaOH+} are the activity coefficients of $CaOH^+$ and Ca^{2+} (using the simulated Ionic Strength) respectively.

$$Ca^{2+} + H_2O = CaOH^+ + H^+ \quad \text{where, } \log k = 10^{-12.78} \quad (16)$$

$$\left[Ca^{2+}\right] + \left[CaOH^+\right] = [Ca_{Total}] \quad (17)$$

$$\frac{\Upsilon_{CaOH^+}.\left[CaOH^+\right]}{\Upsilon_{Ca^{2+}}.\left[Ca^{2+}\right]} = \frac{10^{-12.78}}{10^{-pH}} \quad (18)$$

The calculation of the saturation index of C–S–H also requires knowledge of its solubility product. Various values are reported in the literature corresponding to $CaO-SiO_2-OH$ systems with specific Ca/Si ratios. Values as a function of Ca/Si ratio can be obtained by consideration of the $CaO-SiO_2$ solubility curve published and adapted by several authors [33,34] (Fig. 4) and the widely published relationship [20,35–37] between the Ca/Si ratio of C–S–H as a function of Ca^{2+} (Fig. 5). Mathematical fits to these two sets of data, shown in the respective figures, were used to obtain the solubility product of C–S–H as a function of Ca/Si, as shown in Fig. 6. The solubility product values reported for Jennite ($K_{sp} = 10^{-11.85}$) [31] and Tobermorite ($K_{sp} = 10^{-8.0}$) [38] correspond to Ca/Si ratios of 1.5 and 0.833 respectively are also shown in Fig. 6. This plot indicates that C–S–H is somewhat more soluble than these reference phases as expected for a disordered phase. The line of congruent dissolution of alite (Ca:Si = 3:1) is also shown in Fig. 4 and from the point of intersection of this congruent dissolution line and the $CaO-SiO_2$ solubility line, the Ca/Si ratio of the first product formed can be calculated, which is also indicated on Figs. 5 and 6. However, this first C–S–H is predicted to have a low Ca/Si ratio, which would require silicate chain length more than the dimeric species typically seen at such early stages of hydration [39]. In any case the Ca/Si ratio of the C–S–H quickly evolves to around 1.7 in around 20 min, so small differences between predicted and actual composition will not significantly affect the simulations.

The saturation index of C–S–H was calculated at each step from these data. Precipitation was assumed to occur at the first step where SI_{C-S-H} exceeds 0. Subsequently calcium and silicate ions were removed from the solution to keep $SI_{C-S-H} = 0$. The Ca/Si ratio

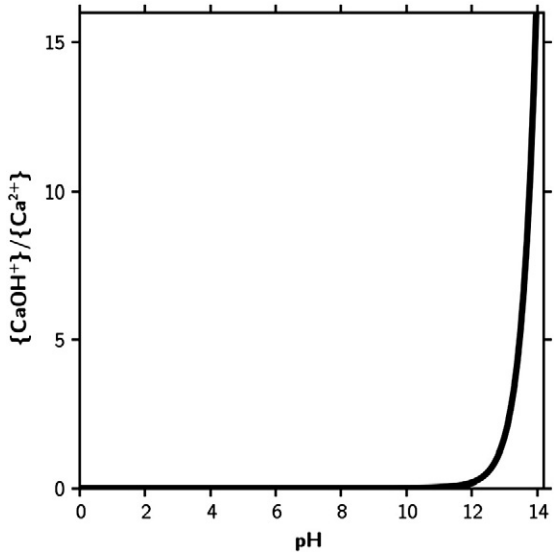

Fig. 3. Ratio of activities of $CaOH^+$ and Ca^{2+} as a function of pH.

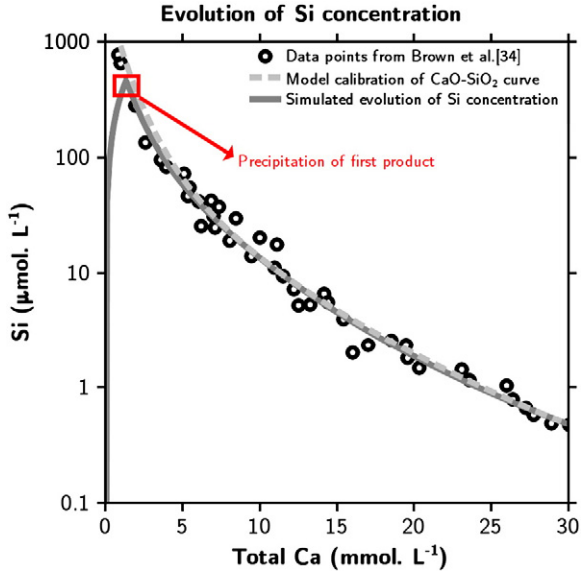

Fig. 4. Solubility curve for C–S–H taken from data of Brown et al. [34]. The dotted line shows the calibration of the SiO_2–CaO solubility data as implemented in the model. The solid line shows the path of solution concentration for congruent dissolution of alite which will intersect the curve at the point indicated by the arrow. From this point and Fig. 5 by using the equivalent total Ca concentration, the composition of the first C–S–H to precipitate can be calculated.

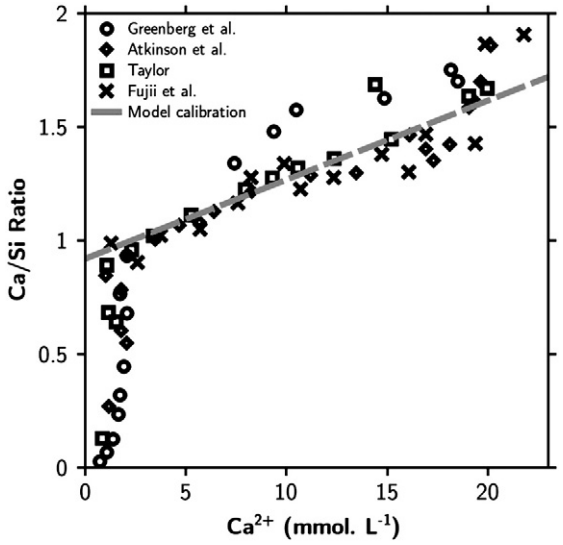

Fig. 5. Evolution of Ca/Si ratio as a function of Ca^{2+} concentration. The calibration of Ca/Si ratio was done using data points (shown as solid symbols) extracted from several authors [20,35–37].

of the product at each step was calculated according to the instantaneous calcium concentration.

It should be noted here, that in the simulations it was approximated that all of Si concentration in the pore solution are considered as $H_2SiO_4^{2-}$. We are aware that the speciation of silica differs from this, including $H_2SiO_4^{2-}$, $H_3SiO_4^-$ and $H_4SiO_4^0$, but at present this can only be calculated iteratively using a system of linear equations and so has not yet been implemented in the computation for reasons of speed.

2.5. Portlandite precipitation

To calculate the Saturation Index of portlandite, Eqs. (19)–(20) were used. K_{sp} at 293.15 K for portlandite was fixed at $10^{-5.18}$, as reported in the PHREEQC thermodynamic database of Parkhurst [32]. The computation of activities of Ca^{2+} and OH^- was implemented in the same way as described in Section 2.4. In the model, portlandite is allowed to precipitate when $SI_{Portlandite}$ reaches a value of 0.40 for the first time, which corresponds to the maximum widely reported in the literature [31,45].

$$SI_{Portlandite} = \log\left(\frac{IAP_{Portlandite}}{K_{sp\ Portlandite}}\right) \tag{19}$$

where,

$$IAP_{Portlandite} = \left\{Ca^{2+}\right\}.\{OH^-\}^{2.0} \tag{20}$$

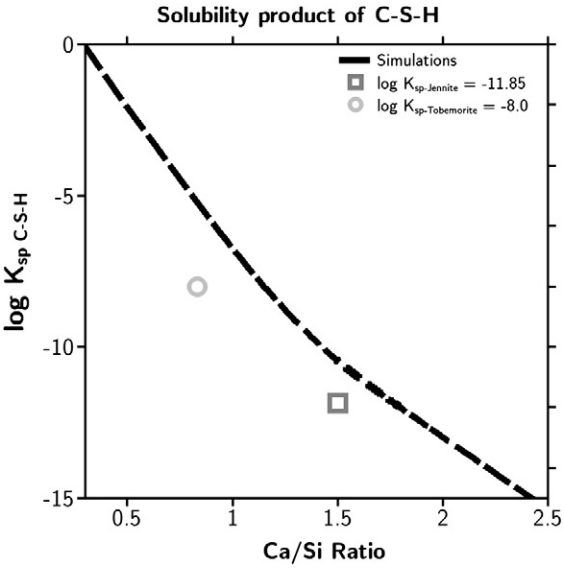

Fig. 6. Simulated plot of log ($K_{sp\ C\text{–}S\text{–}H}$) as a function of Ca/Si ratio. The data points correspond to tobermorite and jennite [31,38]. The point at which first product forms is also indicated.

2.6. Calibration of parameters for SCD regime

As discussed above, the equation controlling the dissolution is described by Eqs. (8a) and (8b). This equation contains 3 parameters:

- k_{diss}: the dissolution rate coefficient in the faster dissolution regime, before the onset of step retreat.
- $c_{step\ retreat}$: equals the assumed constant rate of dissolution per surface area in the step retreat regime.
- β_{max}: the critical degree of undersaturation of alite for onset of the step retreat regime.

These parameters were calibrated iteratively by trying to match the first part of the heat evolution (up to the end of the induction period) from the simulations to the experimental data from isothermal calorimetry. Fig. 7 shows the sensitivity of the output simulation curves during the first few hours to the values of these coefficients. All three values must be defined independently to obtain the correct shape of the experimental heat evolution curves. The value of k_{diss} influences mainly the steepness of the slowdown in dissolution rate, while the parameter $c_{step\ retreat}$ affects the minimum heat evolution during the induction period. The value of β_{max} changes the point of transition from the undersaturation to the step-retreat regime and, consequently, the time spent in the step-retreat regime. At higher values of β_{max}, the dissolution kinetics stay in the fast dissolution regime longer and, hence, consequently, a shorter time in the step retreat regime is required to reach portlandite supersaturation. The reverse happens when the value of β_{max} is lower. The values of all three dissolution parameters affect the time at which portlandite precipitates. These best values obtained are shown in Table 3 are kept constant in all subsequent simulations.

The best value of β_{max} was found to be $10^{-22.0}$. As discussed by Julliand et al. [2] it is seen that the onset of slow dissolution takes place when IAP_{alite} is still many orders of magnitude away from the hypothetical equilibrium solubility for alite[3] between 3 and 1.14×10^{-4} [24,27]. This is depicted in Fig. 8, which shows log ($IAP_{alite}/K_{sp\text{-}alite}$)[4] with respect to time. Once portlandite precipitates (when $SI_{Portlandite}$ reaches a value of 0.40), the concentrations of calcium and hydroxyl ions decrease causing a corresponding decrease in log ($IAP_{alite}/K_{sp\text{-}alite}$) back to the high dissolution regime. Therefore one reason for the acceleration period is due to the transition of the dissolution kinetics back to the high dissolution regime.

The relationship between the dissolution rate and the understauration of alite (log (β_{alite})) is shown in Fig. 9. The dissolution profile of alite comprises of two regimes: Undersaturation below β_{max} in which the rate varies linearly with the difference ($\beta_{max}-\beta_{alite}(t)$) or logarithmically with the Saturation Index; and undersaturation above β_{max} corresponding to the step retreat regime, where rate of dissolution is constant equal to (a_{SSA} . $c_{step\ retreat}$). After the precipitation of portlandite the rate of dissolution increases in magnitude and transitions back to the high dissolution regime. The form of this curve is the same as that proposed by Juilland (Fig. 20 in [2]).[5] The solid symbols on this curve are the

[3] NB it is not possible to precisely measure the equilibrium solubility for alite, due to the precipitation of the hydrate phases. Values between 3 and 10^{-4} are reported.

[4] $\log(IAP_{alite}/K_{sp\text{-}alite}) = \log(\beta_{alite})$.

[5] The values for alite undersaturation in the original paper were not calculated. The values are simple projections which represent the decrease in undersaturation from high values to very low values as dissolution progresses.

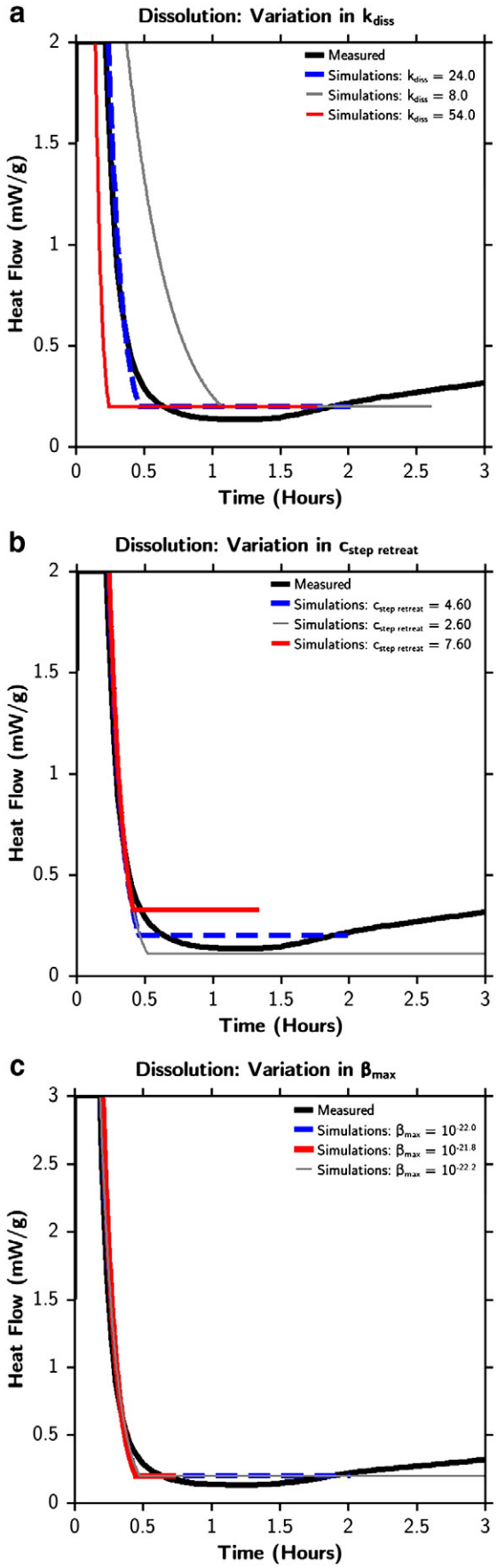

Fig. 7. Sensitivity of the dissolution parameters as indicated at the top of each figure. In all simulations w/c = 0.4 and a_{SSA} = 2000 cm^2/g (Alite C2). The values were calibrated (see Table 3) so as to provide the best fit with the measured heat evolution profile during the dissolution and induction periods. As can be seen, values lower or higher than the calibrated values show deviation from the measured profile.

Table 3
Calibrated values of dissolution parameters at the temperature of 293.15 K.

Dissolution parameters	Values
K_{diss}	24.0 (10^{-6} mol kg m^{-4} s^{-1})
β_{max}	10^{-22} (Unitless)
$c_{step\ retreat}$	4.6 (10^{-29} mol kg m^{-4} s^{-1})

experimental data points from Damidot [25]. It is interesting to note the excellent agreement between the values obtained from this study of alite synthesized by Costoya and the value from a totally independent alite (or C_3S) synthesis by Damidot.

2.7. Evolution of calcium and silicate concentrations and C–S–H during SCD regime

The evolution of the solutions during the SCD regime was examined. Brown [34] provides the most detailed experimental solution data at a w/c ratio close to those used practically in pastes (w/c = 0.7). Fig. 10 shows the simulated evolution of total Si, total Ca and Ca^{2+} concentration with time compared to experimental data reported by Brown.

Figs. 11 shows, the evolution of the Ca/Si ratio of the C–S–H and the total amount of C–S–H formed up to the end of the induction period. It should also be noted that the rate of dissolution of alite is assumed to be unmitigated by the physical precipitation of C–S–H during the early ages. The change in the surface area of particles is also not taken into account in the model during the SCD regime. This, however, has little or no impact on alite dissolution because the amount of C–S–H formed until the end of induction period (shown in Fig. 11b) is very small.

2.8. Nucleation and densifying growth (NDG) regime

A modified form of boundary nucleation and densifying growth mechanism proposed by Bishnoi and Scrivener [3] is used to capture the main heat evolution peak. This is schematically depicted by Fig. 12. Portlandite, outer C–S–H and inner C–S–H are the products which continue to form as the alite dissolves. The average growth of the outer C–S–H phase around the alite grains is represented as a product of low packing density and it forms as the outer layer on alite grains. However, in order to speed up calculations, the equations were modified so that the interaction on the scale of individual particles need not be calculated. In order to do this, the concept of extended volume ($V_{extended}$), used often in nucleation and growth, will be used. $V_{extended}$ represents the expected volume of a set of growing nuclei if the impingements between these nuclei are neglected. Usually, the extended volume is converted to the real volume using Eq. (21):

$$V_{real} = 1 - e^{-V_{extended}} \quad (21)$$

However, this equation holds only for systems with a single product and does not take into account the volume occupied by other products such as portlandite. For such systems, it can be assumed that the probability, and therefore the fraction of the extended volume lost

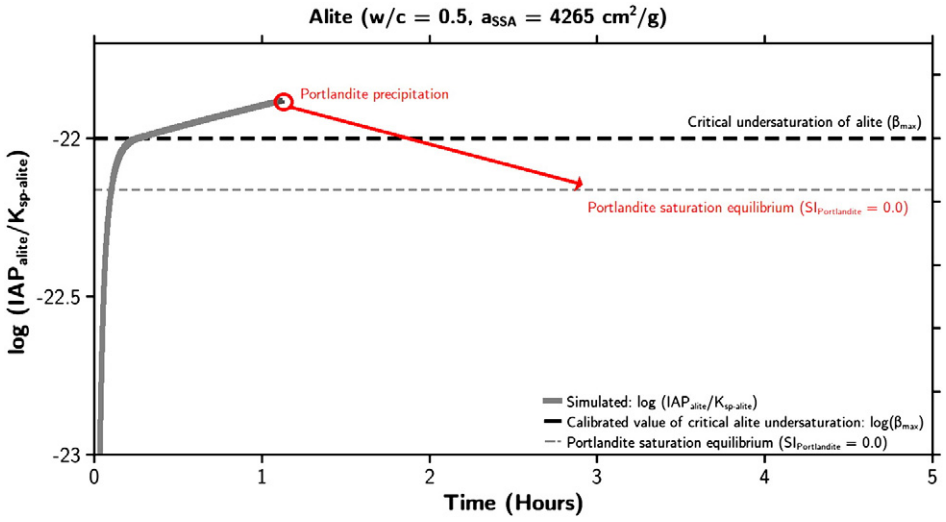

Fig. 8. Simulation evolution of log ($IAP_{alite}/K_{sp\text{-}alite}$) as a function of time. The black dotted line represents the critical undersaturation value (log (β_{max}). The specific surface area and w/c ratio are indicated at the top of the figure. Once portlandite precipitates at the point indicated by the circle symbol, log ($IAP_{alite}/K_{sp\text{-}alite}$) decreases again (shown schematically by the arrow) to the high dissolution regime until portlandite saturation equilibrium is reached. The value of log ($IAP_{alite}/K_{sp\text{-}alite}$) at the point of portlandite solubility equilibrium (indicated by the grey dotted line) was calculated as −22.17.

to overlaps, increases as the real volume available for growth reduces, as shown in Eq. (22).

$$\frac{dV_{real}}{dt} = \frac{dV_{extended}}{dt}(1 - V_{real}) \tag{22}$$

If a densifying growth of C–S–H is assumed, the mass of alite reacting in a period δt can be written as:

$$-\delta m_{alite} = \frac{1}{k}\left[\frac{\rho(t_r)}{\rho_0}\left(dV_{extended,CSH}(t+\delta t) - dV_{extended,CSH}(t)\right)(1 - V_{real}) + \frac{\rho(tr+\delta tr) - \rho(tr)}{\rho_0} V_{real,CSH}\right] \tag{23}$$

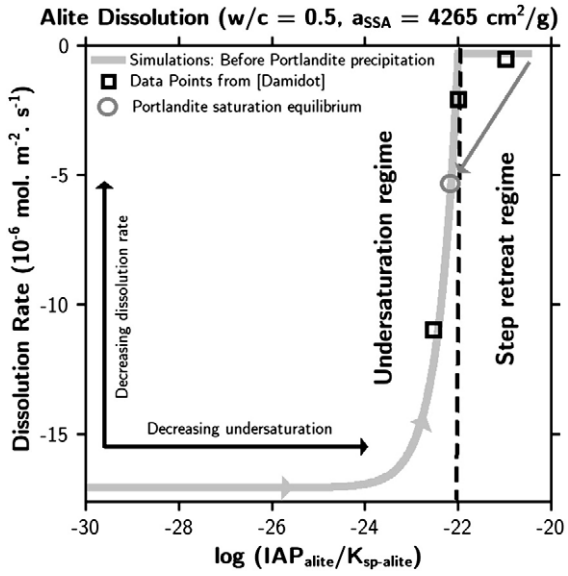

Fig. 9. Dissolution profiles versus undersaturation for alite (as obtained from simulations for w/c = 0.5 and a_{SSA} = 4265 cm^2/g). The round symbols represent measured values from [25]. As portlandite precipitates, ions are consumed and the dissolution kinetics transition back to the undersaturation regime. The decrease is shown schematically by the arrow and the point of portlandite solubility equilibrium (calculated as log ($IAP_{alite}/K_{sp\text{-}alite}$) equal to −22.17) is indicated by the circle.

where k is the ratio of mass of alite reacting to the mass of C–S–H produced. The equation now takes into account both the space occupied by other phases and the change of density of C–S–H which is already present in the system.

$$\text{where: } \textit{Extended volume } (V_{extended}) = \int_0^{G_{out}\cdot t} a_{BV}\cdot\left(1 - \exp\left(-A_f\right)\right) dy \tag{24}$$

Where A_f can be written as:

$$A_f = \pi\left[I_{density}.G_{par}^2\left(t_r^{\,2} - \frac{y^2}{G_{out}^2}\right) + I_{rate}.G_{par}^2\left(\frac{2y^3}{3G_{out}^3} + \frac{t_r^{\,3}}{3} - \frac{y^2 t_r}{G_{out}^2}\right)\right] \tag{25}$$

where, G_{out} (μm h^{-1}) and G_{par} are the outward and parallel growth rates of outer C–S–H, t_r (hour) is the age of the product, I_{rate} (μm^{-2} h^{-1}) is the rate of nucleation per unit area of the untransformed boundary and $I_{density}$ (μm^{-2}) is the nucleation density of the product. Eq. (25) can also be expressed using N_{rate} and $N_{density}$ which are respectively the products of the nucleation rate and the nucleation density with the square of the parallel growth rate ($I_{rate}G_{par}^2$ and $I_{density}G_{par}^2$). The dependence of the density of C–S–H on time can be written as below:

$$\rho\,(t_r) = \rho_{max} - (\rho_{max} - \rho_{min})\cdot\exp\left(\frac{-k_{den}.t_r}{(\rho_{max} - \rho_{min})}\right) \tag{26}$$

where ρ_{max} (g cm^{-3}) is the final density of outer C–S–H, ρ_{min} (gm cm^{-3}) is the initial density of outer C–S–H, k_{den} (g cm^{-3} h^{-1}) is the rate of densification of outer C–S–H and a_{BV} is the total surface area of alite powder per unit volume (μm^{-1}). In order to compute the values of a_{BV}, the total specific surface area of the particles a_{SSA} (cm^2/g), as measured from experimental techniques, were used as inputs and the dimensions were transformed to (μm^{-1}) using the density value of alite of 3.15.

2.9. Sensitivity of the NDG parameters

In order to illustrate the sensitivity of the NDG parameters, simulations were implemented with a base value of the parameters as shown in Table 4.0. The parameters were then varied individually

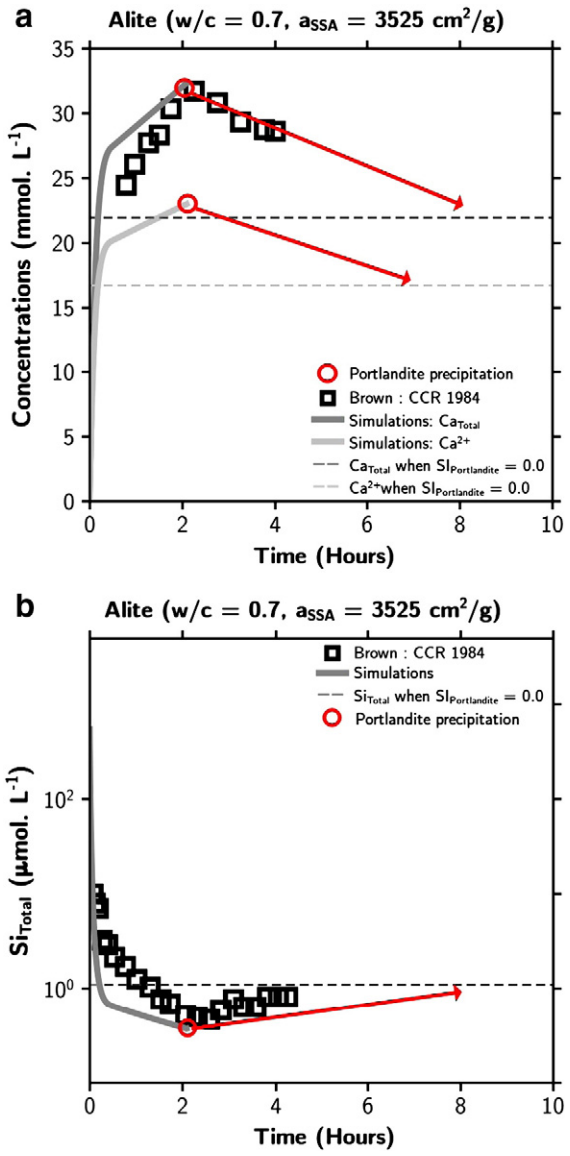

Fig. 10. Evolution of concentration (a) Total Calcium and Ca^{2+} (b) Total Si. In the model it is assumed that all of Si concentration exists as $H_2SiO_4^{2-}$. Once portlandite precipitates, Ca_{Total} and Ca^{2+} decrease and Si_{Total} increases until portlandite solubility equilibrium is reached (shown by arrows). The levels of Ca^{2+}, Ca_{Total} and Si_{Total} at portlandite solubility equilibrium are indicated by dotted lines. The data points have been extracted from [34].

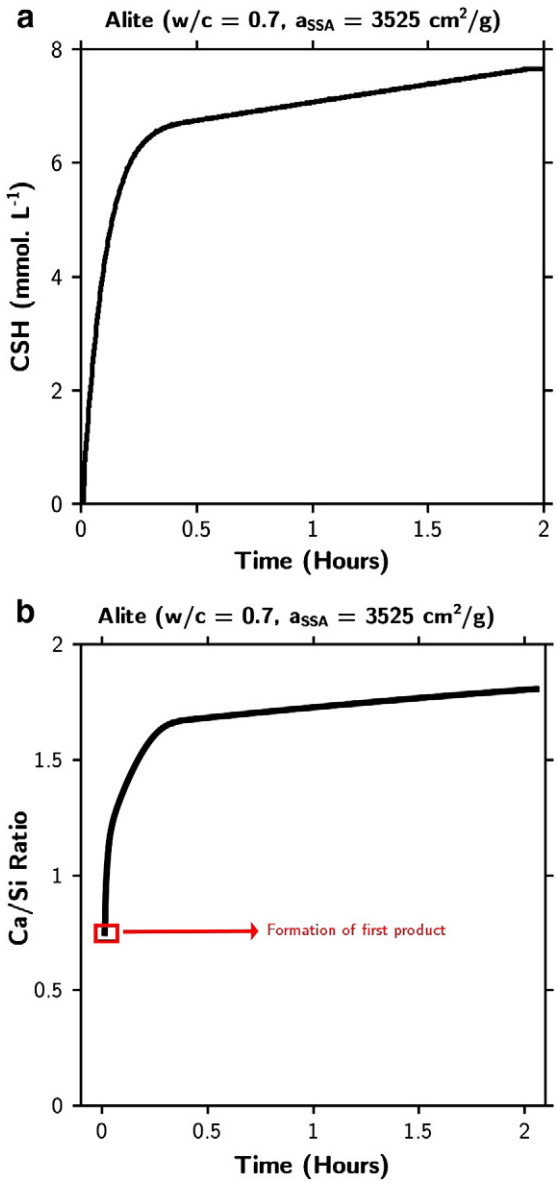

Fig. 11. Simulated time dependent evolution of (a) Ca/Si ratio of C–S–H (b) amount of C–S–H until the end of the induction period.

while preserving the value of the other parameters to show the influence of the variable on the overall kinetics. The simulated plots with variations of the parameters ρ_{min}, G_{out}, k_{den}, G_{par}, I_{rate} and t_0 are shown in Fig. 13. As can be seen, each parameter affects the heat evolution profile in a unique fashion. In the subsequent simulations, small variations in G_{par}, k_{den}, ρ_{min}, and I_{rate} parameters are required in addition to a major variation in the G_{out} parameter to capture the reaction kinetics of alite systems with different particle sizes.

3. Simulating different particle size distributions

In the following section, the results of simulations are presented. Simulations were implemented for the different particle size distributions of alite investigated by Costoya [41] and Bazzoni [42]. This consists of 6 particle size distributions from the same protocols of synthesis of alite described in Table 5 and Fig. 14. The PSD of the original alite powder, Alite-C2, is close to that cement. The other narrow PSDs were chosen to cover the entire range of particle sizes present in cement. The water to cement ratio was fixed at 0.4. All samples were mixed

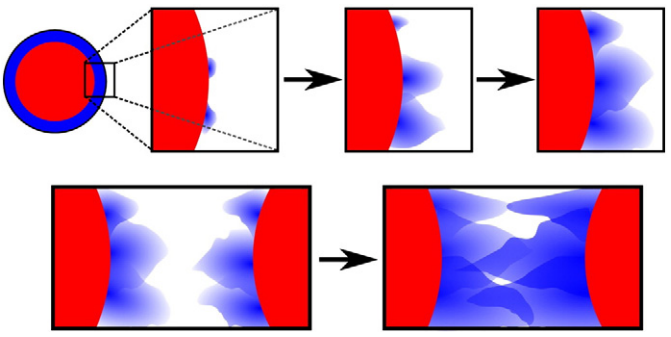

Fig. 12. Diffuse growth of C–S–H as the microstructural volume as it densifies. Single particle (top) and between particles (bottom).

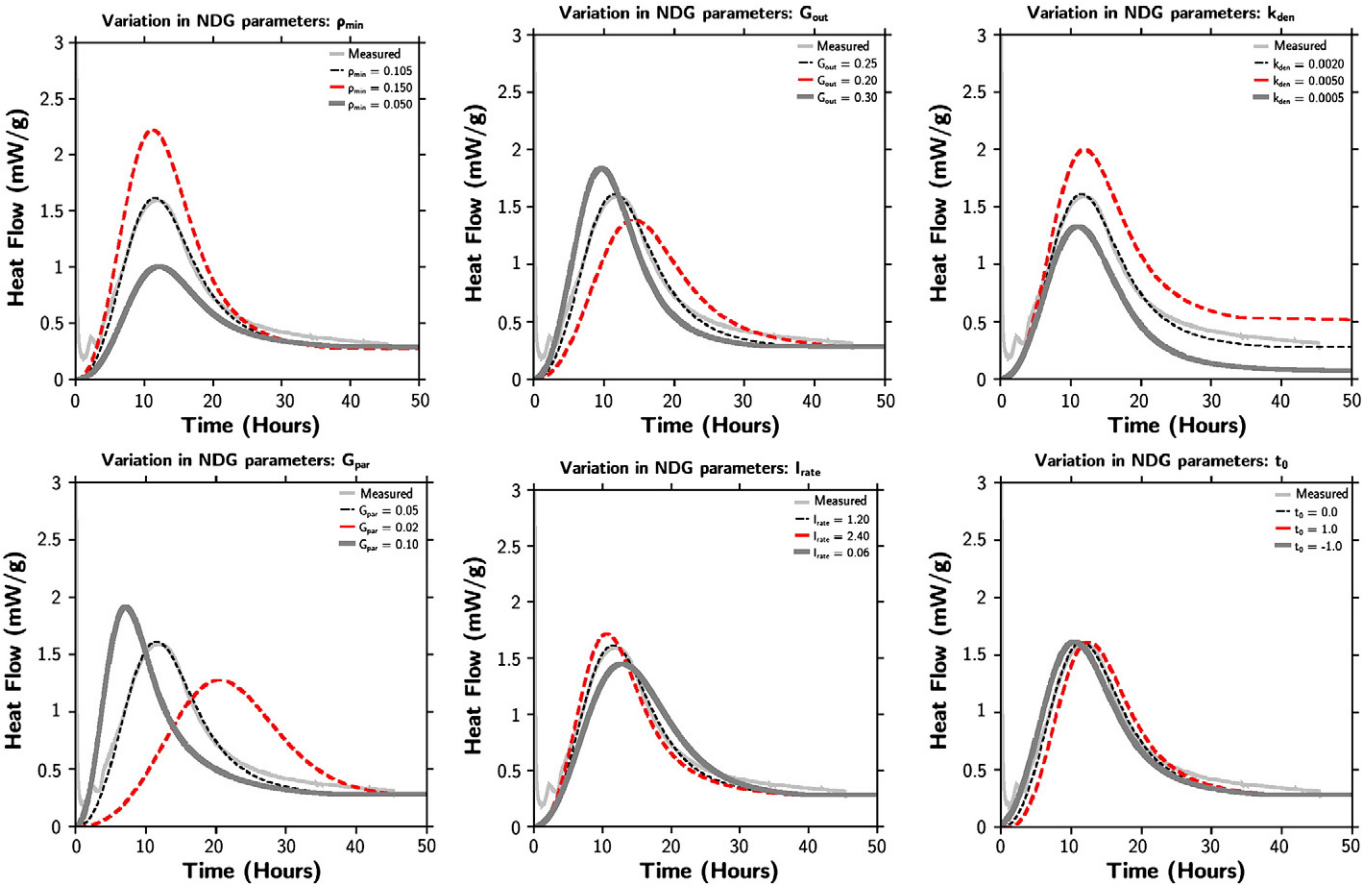

Fig. 13. Sensitivity of the parameters ρ_{min}, G_{out}, k_{den}, G_{par}, I_{rate} and t_0 in the NDG regime. The variable parameter is indicated at the top of each figure.

externally and then placed in a TamAir isothermal calorimeter. The heat evolution profiles were measured at a constant temperature of 293.15 K. Although some of the initial heat evolution peak is missed, this is only about 5 min from addition of water.

In all simulations, the calibrated dissolution parameters were used without any change. The parameters of the nucleation and growth kinetics were varied to obtain the best fit and their values are shown in Table 6.

The main parameter from the different PSDs in the simulation is the total surface area, which has a direct impact on the rate of dissolution as described by Eq. (8). The measured and simulated heat evolution profiles are shown in Figs. 15 (early ages) and 16 (up to 30 h). It can be seen that across the range of PSDs the simulation is able to well capture the slowdown in reaction rate and the induction period with the same parameters for the dissolution kinetics. The acceleration regime starts early for alite systems with finer

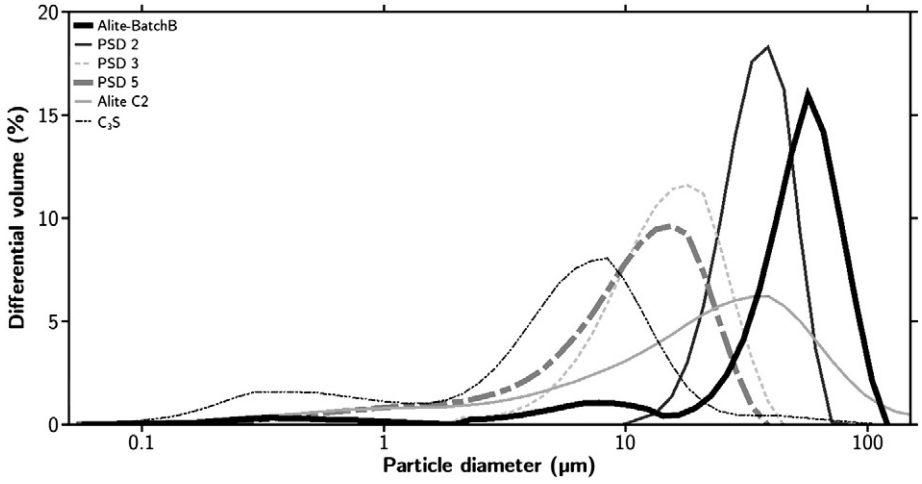

Fig. 14. Measured particle size distributions of all alite systems presented in this study. Other details about the PSDs can be found in Table 5.

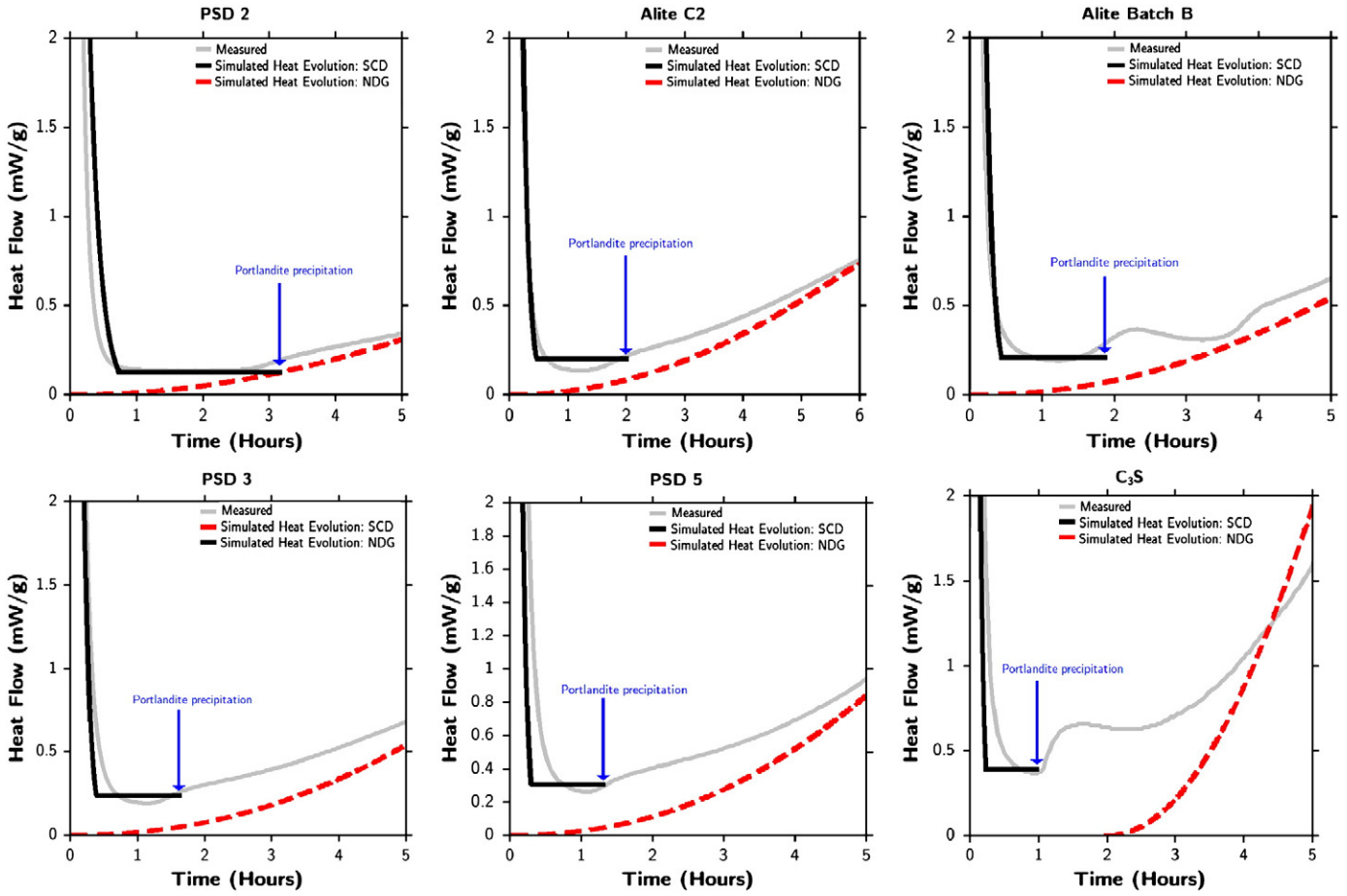

Fig. 15. Simulated and Measured heat flow rates for alite systems with different PSDs for the first 5 h w/c ratio for these systems is 0.40 and the PSDs are indicated at the top of each figure. In each plot, the solid black and dotted lines represent heat flow rates obtained using the SCD and NDG mechanisms respectively. The termination points of the solid black lines represent the end of the simulated induction period and precipitation of portlandite. The full plots shown in Fig. 16 are obtained by combining the heat flow rates obtained from the two mechanisms.

particles and later for coarser particles. Fig. 17 shows the evolution of Ca^{2+} concentration and $SI_{Portlandite}$ in the pore solution as simulated in the model. As can be seen, the times at which $SI_{Portlandite}$ exceeds 0.4 for the first time changes as PSD changes and these times are approximately the same as the times at which the rate of reaction begins to accelerate in the measured calorimetry plots.

The variation in the NDG parameters is discussed in Section 3.1.

3.1. Variation in simulation parameters

The NDG parameters with largest variations in the simulations are G_{out}, which represents the outward growth rate of C–S–H, and I_{rate}, which is the rate of nucleation of C–S–H per unit area. The variation in the rest of the parameters is small. The values of ρ_{min} and k_{den} for alite are similar but the largest variations are found for C_3S. This deviation can be attributed to differences in the intrinsic reactivities and specific surface area values between C_3S and alite. It must also be stated here that the need to vary four of the NDG parameters is unique to systems in which the surface area of alite particle changes drastically. The number of variable parameters is reduced to 2 when simulations are implemented for the same PSD while studying the variation of other process parameters, as demonstrated in other studies [44].

The values of I_{rate} were compared to the specific surface area of the particles as shown in Fig. 18. It was observed that I_{rate} increases with increasing specific surface area of the particles. It appears that smaller particles have higher nucleation rates, despite being normalized for surface area. The exact reasons for this are unclear, although it may be related to the fact that smaller particles have undergone more "grinding action" and so may have a more highly damaged surface. It is also seen that C_3S has a lower nucleation rate, again the reasons for this are unclear at this stage.

The values of G_{out} were compared to the average distance between closest neighboring particles and the specific surface area of the particles as shown in Fig. 19. As can be seen, G_{out} decreases as the specific surface area of the particles increases (Fig. 19a). Interestingly this corresponds to an increase in direct proportion to the distance between the particles (Fig. 19b). The variation of G_{out} with respect to the initial inter-particle space suggests an opportunistic growth of the hydrates according to the available space in the microstructure, the exact mechanism is not known. It may, however, be speculated that this variation is due to slight concentration gradients in the immediate vicinity of particles.

4. Transition from SCD to NDG mechanism

In the model, the SCD regime and the simulated induction period are terminated at the point of portlandite precipitation. The kinetics beyond the end of the induction period is simulated

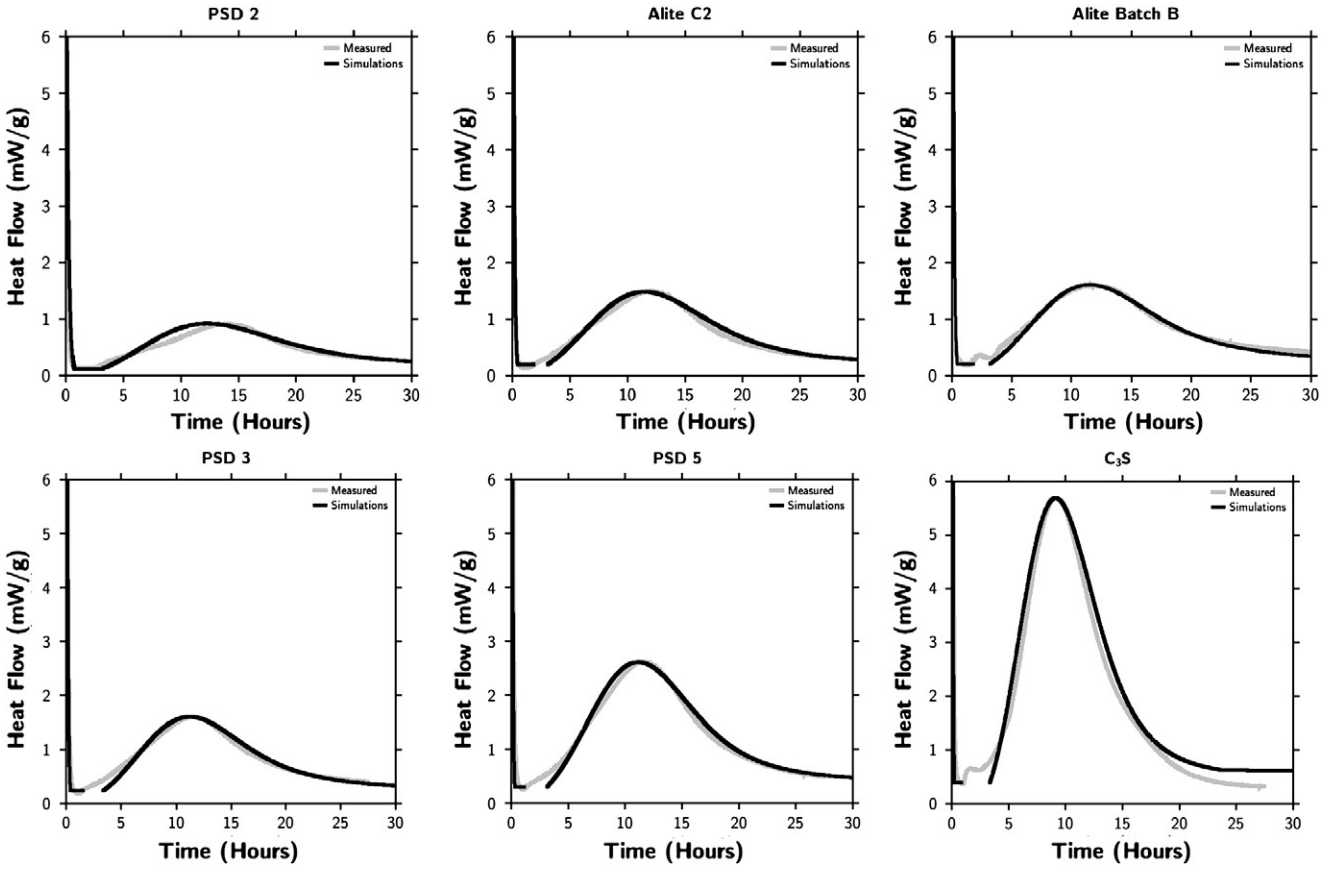

Fig. 16. Measured and simulated rate of heat released for alite systems up to 30 h of hydration. w/c ratio of all systems is 0.40.

using NDG kinetics (as depicted in Fig. 2b). But this leaves a gap between the end of the simulated induction period and the acceleration period (shown in Fig. 20). The transition between the two regimes is captured in the following manner:

- Until the end of the induction period, the SCD mechanism is used. Heat-flow rate during this period is calculated using only SCD kinetics.
- NDG kinetics is implemented in parallel and independent of the SCD kinetics. The parameters for the NDG kinetics include a start time parameter (t_0) which is determined to best fit the measured calorimetry curve. The heat-flow rate obtained from NDG kinetics is calculated and stored but not used to compute the overall hydration rate until the SCD regime is terminated.
- When portlandite reaches a supersaturation value of 0.40, precipitation of this phase occurs. At this point the SCD regime (and the simulated induction period) is terminated. From this point, calcium and hydroxyl ions decrease from portlandite supersaturation value of 0.40 to the equilibrium value of 0.00. If this decrease in the concentrations is implemented in a single step, the rate of dissolution increases dramatically as indicated in Fig. 20. In the simulations presented in this study (Figs. 15 and 16), the decrease is implemented in a single time-step. However, experimentally [34,45] it is observed that this drop in concentrations is progressive over a few hours. Therefore, a simple fit function was used, shown in Eq. (27) (according to observations of pore-solution concentration data from literature [34,45]) to give a gradual decrease from portlandite supersaturation to portlandite solubility equilibrium.

$$\mathrm{Ca}(t) = \mathrm{Ca}_{eq} + \left(\left(\mathrm{Ca}_{SS} - \mathrm{Ca}_{eq} \right) \cdot \exp\left(\frac{r_{Ca} \cdot \left(t - t_{precipitation} \right)}{\left(\mathrm{Ca}_{SS} - \mathrm{Ca}_{eq} \right)} \right) \right) \quad (27)$$

where, Ca(t) is the concentration of total calcium, Ca_{eq} is the total calcium at portlandite solubility equilibrium, Ca_{SS} is value of calcium concentration at the portlandite supersaturation of 0.40, t is the time, $t_{precipitation}$ is the time at which portlandite precipitates and r_{Ca} is a fit constant that depends on a_{SSA} and w/c ratio. Fig. 21 shows the simulated evolution of calcium concentrations and the resulting heat-evolution profiles using both sudden and progressive decrease in the concentrations. The heat evolved during the transition is calculated using Eq. (4). Using this criterion, the bump at the end of the induction period [40] can be reproduced (shown in Fig. 21b).

- Since the NDG kinetics are implemented independent of the SCD kinetics, the heat-flow rate calculated from the NDG kinetics remains unaltered at the point of portlandite precipitation. As can be seen in Fig. 20, at this point, the heat-flow rate from NDG kinetics is lower that the heat-flow rate from SCD kinetics. The controlling mechanism is switched to NDG kinetics only when the heat-flow rate from this mechanism becomes equal to that of the SCD mechanism at the termination point. Due to this, in the simulations there is a gap between the two regimes, as can be seen in the simulations (Figs. 15 and 16).

5. Simulation of solution evolution with different starting solutions

It was seen in the simulation of our experimental data that the dissolution parameters remained the same for all conditions and the

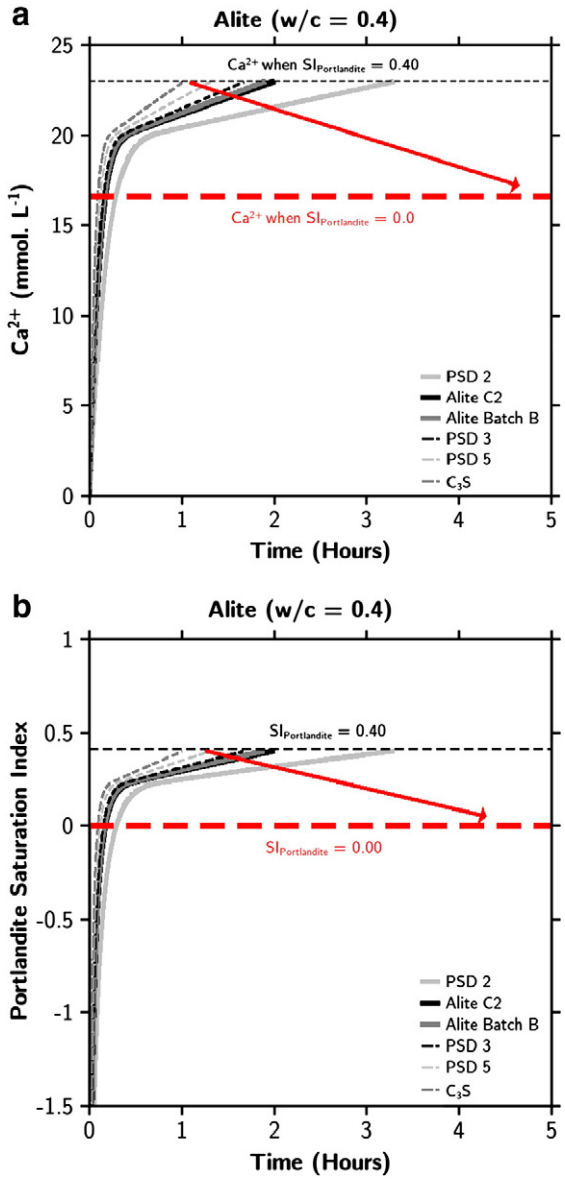

Fig. 17. Evolution of (a) Ca^{2+} concentration (b) $SI_{Portlandite}$. Once portlandite precipitates, the Ca^{2+} concentration $SI_{Portlandite}$ values decrease (schematically shown by arrows) until portlandite solubility equilibrium is reached (indicated by the dotted lines). In all systems, w/c = 0.40.

kinetics are determined only by the build-up of ions in solution. In addition it was seen in Section 2.7 that the data of Brown for alite hydration could also be well captured by the same parameters. To explore this further, the impact of the composition of the starting solution was studied by simulation and compared to the data of Brown [45] for staring solution of saturated DI-water, calcium hydroxide, sodium hydroxide and sodium chloride. For all systems, the input parameters included: w/c ratio, initial Ionic strength, initial pH and initial Ca concentration, as shown in Table 7. Calibrated dissolution parameters were used, as shown in Table 3. The results of the simulations are shown in Fig. 22. As discussed in Section 2.7, it should be noted that the Calcium concentrations provided by Brown correspond to the total Calcium concentration NOT Ca^{2+}. In the measured and simulated curves, the point of portlandite precipitation (indicated by circular symbols) is marked by the decrease (shown by the arrows) in the total Ca concentration. As can be seen, the levels of total Ca concentration at supersaturation and near equilibrium

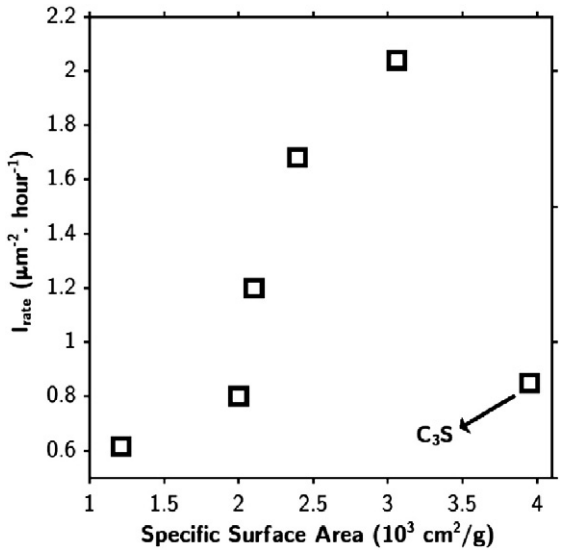

Fig. 18. Variation of the nucleation rate (I_{rate}) in the model with respect to the specific surface area of the PSD.

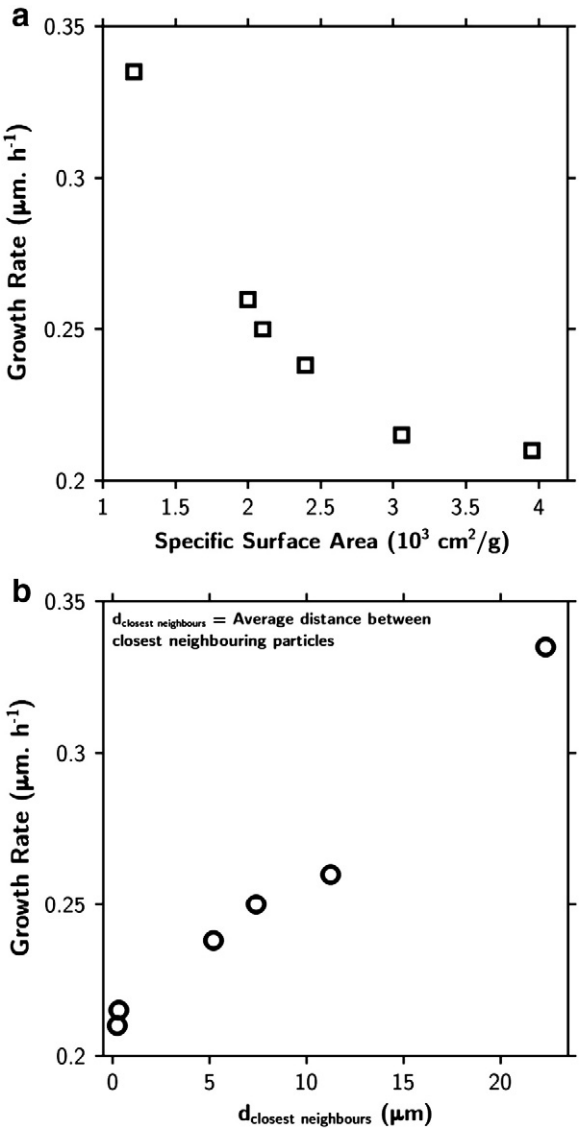

Fig. 19. Variation of the Outward growth rate (G_{out}) in the model with respect to (a) specific surface area of the PSD (b) Average distance between closest neighboring particles.

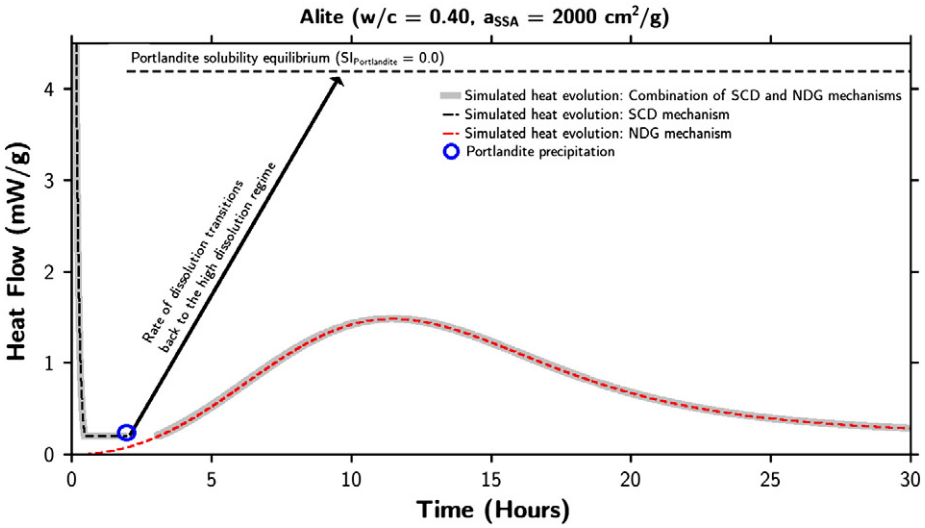

Fig. 20. Simulated evolution of heat flow using SCD, NDG and combinations of SCD and NDG mechanisms. As can be seen, once portlandite precipitates, dissolution transitions to the high-dissolution regime rendering NDG as the slower and rate determining process. The switch from SCD to NDG mechanism is made when the heat flow rates from both regimes equalize.

Table 4
Base values and short description of the parameters used for the simulations shown in Fig. 13.

Parameters and base values	Description
Nucleation density ($I_{density}$) = 8.0 (μm^{-2})	Number of nuclei of C–S–H per unit area
Outward Growth rate (G_{out}) = 0.25 ($\mu m\ h^{-1}$)	Outward Growth rate of the nuclei of the product
Parallel Growth rate (G_{par}) = 0.05 ($\mu m\ h^{-1}$)	Growth rate of the nuclei along the surface
Nucleation rate (I_{rate}) = 1.20 (μm-2 h^{-1})	Rate of nucleation of C–S–H per unit ar
Initial C–S–H density (ρ_{min}) = 0.105 (gm cm^{-3})	Initial packing density of outer C–S–H.
Final C–S–H density (ρ_{max}) = 2.10 (gm cm^{-3})	Final packing density of outer C–S–H
Rate of densification (k_{den}) = 0.0020 (gm $cm^{-3}\ h^{-1}$)	Rate of densifictation of outer C–S–H
Base density of C–S–H (ρ_0) = 2.10 (gm cm^{-3})	Density of Inner C–S–H
Starting time (t_0) = 0.0	Start time of NDG

Table 5
Median size, Specific surface area and density values of all alite gradations used in this study. The specific surface area values are reported as per the values of blaine fineness obtained experimentally using laser diffraction.

PSD	D_{modal} (μm)	Specific surface area (cm^2/g)	Density (g/cm^3)
Alite C2	33	2000	3.15
Alite-Batch B	32	2100	3.14
PSD 2	38	1212	3.15
PSD 3	18	2393	3.17
PSD 5	13	3059	3.15
C3S	6	3952	3.15

Table 6
Values of the NDG parameters used for the simulations.

PSDs	a_{SSA}	ρ_{min}	I_{rate}	$I_{density}$	G_{par}	G_{out}	k_{den}	t_0
AliteC2	2000	0.105	0.800	8.00	0.0500	0.260	0.0015	0.0
PSD 3	2393	0.097	1.680	8.00	0.0500	0.238	0.0020	0.0
PSD 5	3059	0.148	2.040	8.00	0.0500	0.215	0.0035	0.0
C3S	3952	0.290	0.850	8.00	0.0968	0.210	0.0050	2.0
Alite-Batch B	2100	0.105	1.200	8.00	0.0500	0.250	0.0020	0.0
PSD 2	1212	0.073	0.615	8.00	0.0403	0.335	0.0010	0.0

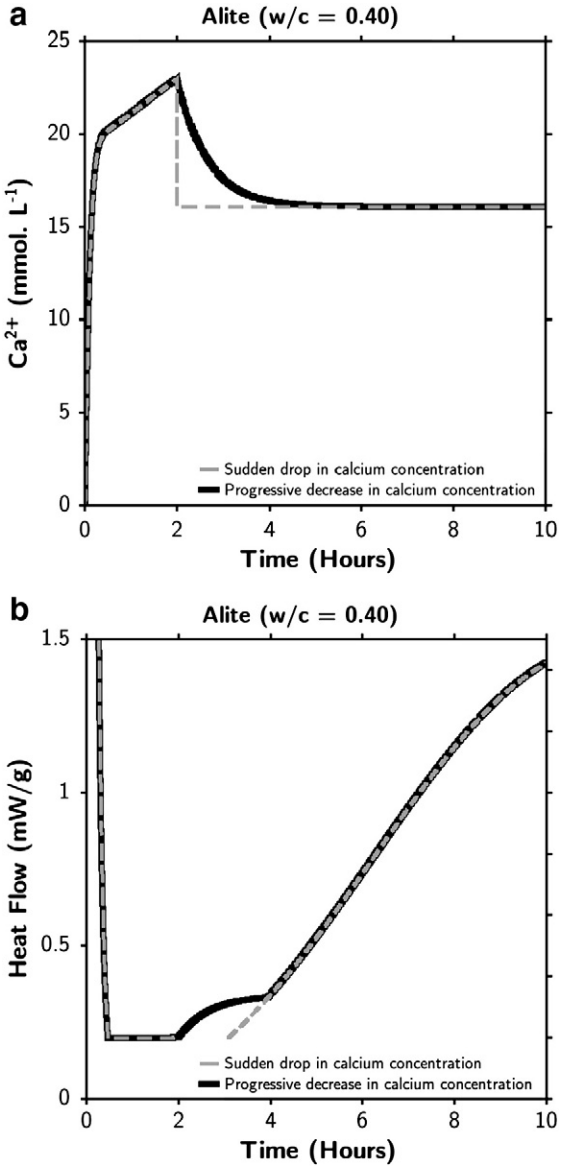

Fig. 21. (a) Calcium concentration evolution (b) Heat evolution rates using sudden and progressive decrease in the concentrations of calcium.

Table 7
Input parameters for simulations shown in Fig. 22 for systems from [45]. The parameters represent the initial state of the system. The dissolution parameters used for these simulations are shown in Table 3. The w/c for all systems is 2.0.

Solution	pH	Ionic strength (mol L^{-1})	OH^- concentration (mol L^{-1})	Ca concentration (mol L^{-1})
DI-water	7.00	0.0000	0.0000	0.000
NaCl solution	6.98	0.0408	0.0000	0.000
$Ca(OH)_2$ solution	12.45	0.0633	0.0422	0.0211
NaOH solution	12.68	0.0408	0.0408	0.000

and the time of portlandite precipitation are well-captured, thus validating the implementation of the solubility calculations in the model.

This effect of starting solution concentration is further discussed in another article (Juilland et al. [43]), where the effect of mixing is studied.

6. Conclusions

It is shown in this paper that the hydration of alite can be well simulated on a quantitative basis by 2 mechanisms: Solution controlled dissolution (SCD) up to the end of the induction period and nucleation with densifying growth (NDG) to capture the main heat evolution peak. It is found that there is a gap between the two simulations regimes, which corresponds to a "bump" in the calorimetry curves. We conjecture that this bump corresponds to an increase in the dissolution rate of alite when portlandite precipitates due to an increase in the alite undersaturation. Subsequently, it seems that the growth of C–S–H takes over as the rate controlling reaction, when the curves can be fitted by the NDG mechanism.

The dissolution parameters of the model calibrated from one particle size distribution are shown to apply well across a range of PSDs. Furthermore it is found that the same values can simulate well results in the literature from other alite and C_3S preparations. Amongst the NDG parameter, the largest variation was found in the outward growth rate and nucleation rate parameters which correlate with the distance between particles and initial specific surface area respectively.

Acknowledgments

The authors gratefully acknowledge the financial support from the Swiss National Science Foundation (FNS). The authors thank Dr. Barbara Lothenbach, Dr. Patrick Julliand and Professor Gaurav Sant for discussion and comments while devising the model. The authors also thank Dr. Mercedes Costoya and Amelie Bazzoni for providing the experimental results.

References

[1] S. Bishnoi, K.L. Scrivener, μic: a new platform for modelling the hydration of cements, Cement Concr. Res. 39 (2009) 266–274.
[2] P. Juilland, E. Gallucci, R. Flatt, K.L. Scrivener, Dissolution theory applied to the induction period in alite hydration, Cement Concr. Res. 40 (2010) 831–844.
[3] S. Bishnoi, K.L. Scrivener, μic: studying nucleation and growth kinetics of alite hydration using μic, Cement Concr. Res. 39 (2009) 849–860.
[4] J.W. Bullard, H.M. Jennings, R.A. Livingston, A. Nonat, G.W. Scherer, J.S. Schweitzer, K.L. Scrivener, J.J. Thomas, Mechanisms of cement hydration, Cement Concr. Res. (2010), http://dx.doi.org/10.1016/j.cemconres.2010.09.011.

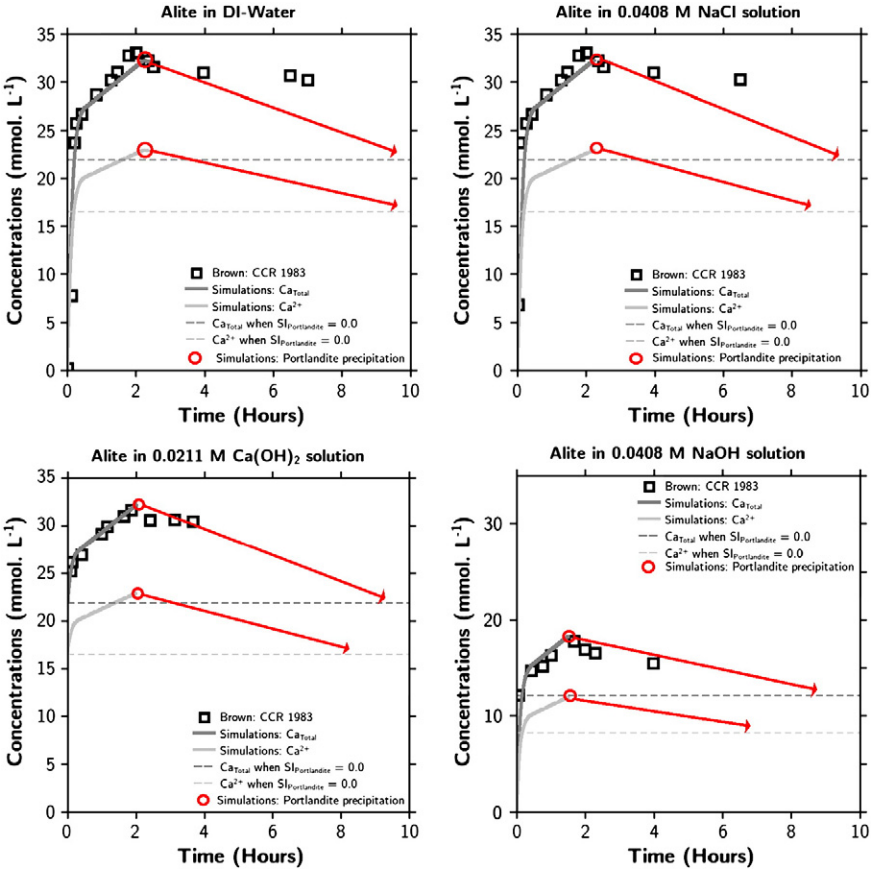

Fig. 22. Simulated and measured evolutions of total Ca concentration and Ca^{2+} in alite systems with different initial states of pore solution. Once portlandite precipitates, the Ca^{2+} concentration $SI_{Portlandite}$ values decrease (schematically shown by arrows) until portlandite solubility equilibrium is reached (indicated by the dotted lines) data from [45].

[5] A.C. Lasaga, A. Lüttge, Variation of crystal dissolution rate based on a dissolution stepwave model, Science 291 (2001) 2400–2404.
[6] A. Lüttge, Crystal dissolution kinetics and Gibbs free energy, Journal of Electron Spectroscopy and Related Phenomena 150 (2006) 248–259.
[7] J.J. Thomas, A new approach to modeling the nucleation and growth kinetics of tricalcium silicate hydration, J. Am. Ceram. Soc. 90 (2007) 3282–3288.
[8] J.J. Thomas, J.J. Biernacki, J.W. Bullard, S. Bishnoi, J.S. Dolado, G.W. Scherer, A. Luttge, Modeling and simulation of cement hydration kinetics and microstructure development, Cement Concr. Res. 41 (2011) 1257–1278.
[9] S. Garrault, A. Nonat, Hydrated layer formation on tricalcium and dicalcium silicate surfaces: experimental study and numerical simulations, Langmuir 17 (2001) 8131–8138.
[10] R. Kondo, S. Ueda, Kinetics of hydration of cements, Proceedings of the 5th international symposium on chemistry of cement, Tokyo, 1968, pp. 203–248.
[11] D.P. Bentz, Modelling cement microstructure: pixels, particles, and property prediction, Materials and Structures 32 (1999) 187–195.
[12] J.W. Bullard, A determination of hydration mechanisms for tricalcium silicate using a Kinetic Cellular Automaton Model, J. Am. Ceram. Soc. 91 (2008) 2088–2097.
[13] K. van Breugel, Numerical simulation of hydration and microstructure development in hardening cement-based materials (1): Theory, Cement Concr. Res. 25 (1995) 319–331.
[14] J.W. Bullard, R.J. Flatt, New insights into the effect of calcium hydroxide precipitation on the kinetics of tricalcium silicate hydration, J. Am. Ceram. Soc. 93 (2010) 1894–1903.
[15] T. Knudsen, Modelling hydration of portland cement: the effect of particle size distribution, Proceedings of the Engineering Foundation Conference, 1983.
[16] K.G. McCurdy, Suspension hydration of C_3S at constant pH. I. Variation of particle size and C_3S content, Cement Concr. Res. 3 (1973) 247–262.
[17] S. Garrault, T. Behr, A. Nonat, Formation of the C–S–H layer during early hydration of tricalcium silicate grains with different sizes, J. Phys. Chem. 110 (2006) 270–275.
[18] H.M. Jennings, L.J. Parrott, Microstructural analysis of hardened alite paste, Part II: Microscopy and reaction products, J. Mater. Sci. 21 (1986) 4053–4059.
[19] K. Scrivener, The microstructure of concrete, in: J.P. Skalny (Ed.), Materials Science of Concrete I, American Ceramic Society, Columbus, Ohio, 1989, pp. 127–161.
[20] H.F.W. Taylor, Cement Chemistry, 1st edition Thomas Telford Publishing, 1990.
[21] I. Odler, Chapter 6: Hydration, setting and hardening of Portland cement, in: Peter C. Hewlett (Ed.), LEA's Chemistry of Cement and Concrete, Arnold, London, 2001, pp. 241–298.
[22] J.W. Bullard, A Three-Dimensional microstructural model of reactions and transport in aqueous mineral systems, Modelling and Simulation in Materials Science and Engineering 15 (2007) 711–738.
[23] M.S. Beig, A. Luttge, Albite dissolution kinetics as a function of distance from equilibrium: implications for natural feldspar weathering, Geochim. Cosmochim. Acta 70 (2006) 1402–1420.
[24] F. Bellmann, D. Damidot, B. Moser, J. Skibsted, Improved evidence for the existence of an intermediate phase during hydration of tricalcium silicate, Cement Concr. Res. 40 (2010) 875–884.
[25] D. Damidot, F. Bellmann, B. Möser, T. Sowoidnich, Investigation of the early dissolution behaviour of C_3S, 12th International Congress on the Chemistry of Cement, Montreal, Canada, paper W1-06.5, 2007, 8.-13.7.
[26] L. Nicoleau, Personal Communication.
[27] H.N. Stein, Thermodynamic considerations on the hydration mechanisms of Ca_3SiO_5 and $Ca_3Al_2O_6$, Cement Concr. Res. 2 (1972) 167–177.
[28] A.H. Truesdell, B.F. Jones, WATEQ, a computer program for calculating chemical equilibria of natural waters, Journal of Research, U.S. Geological Survey 2 (1974) 233–274.
[29] D. Rothstein, J.J. Thomas, B.J. Christensen, H.M. Jennings, Solubility behavior of Ca-, S-, Al-, and Si-bearing solid phases in Portland cement pore solutions as a function of hydration time, Cement Concr. Res. 32 (2002) 1663–1671.
[30] F.P. Glasser, E.E. Lachowski, D.E. Macphee, Compositional model for calcium silicate hydrate (C–S–H) gels, their solubilities, and free energies of formation, J. Am. Ceram. Soc. 70 (1987) 481–485.
[31] B. Lothenbach, F. Winnefeld, Thermodynamic modelling of the hydration of Portland cement, Cement Concr. Res. 36 (2006) 209–226.
[32] D.L. Parkhurst, C.A.J. Appelo, PHREEQC 2: a Computer Program for Speciation, Batch-reaction, One-dimensional Transport and Inverse Geochemical Calculations, USGS, Denver, 2001.
[33] H.M. Jennings, Aqueous solubility relationships for two types of calcium silicate hydrate, J. Am. Ceram. Soc. 69 (1986) 614–618.
[34] P.W. Brown, E. Franz, G. Frohnsdorff, H.F.W. Taylor, Analyses of the aqueous phase during early C_3S hydration, Cement Concr. Res. 14 (1984) 257–262.
[35] S.A. Greenberg, T.N. Chang, Investigations of the colloidal hydrated calcium silicates II. Solubility relationships in the calcium oxide–silica–water system at 25 °C, J. Phys. Chem. 69 (1965) 182–188.
[36] K. Fuji, W. Kondo, Heterogeneous equilibrium of calcium silicate hydrate in water at 30 °C, Journal of Chemical Society, Dalton Transaction 2 (1981) 645–651.
[37] A. Atkinson, J.A. Hearne, C.F. Knights, Aqueous Chemistry and Thermodynamic Modelling of $CaO–SiO_2–H_2O$ Gels, AERE R 12548, UKAEA, 1987.
[38] B. Lothenbach, T. Matschei, G. Möschner, F.P. Glasser, Thermodynamic modelling of the effect of temperature on the hydration and porosity of Portland cement, Cement Concr. Res. 38 (1) (2008) 1–18.
[39] J.J. Chen, J.J. Thomas, H.F.W. Taylor, H.M. Jennings, Solubility and structure of calcium–silicate–hydrate, Cement Concr. Res. 34 (2004) 1499–1519.
[40] I. Odler, J. Schuppstuhl, Early hydration of tricalcium silicate III. Control of the induction period, Cement Concr. Res. 11 (1981) 765–774.
[41] M.M. Costoya, Effect of particle size on the hydration kinetics and microstructural development of tricalcium silicate, Doctoral Thesis, Ecole Polytechnique Federale de Lausanne, Switzerland 2008.
[42] Amelie Bazzoni, Personal Communication.
[43] P. Juilland, A. Kumar, E. Gallucci, R. Flatt, K.L. Scrivener, Effect of mixing on early hydration of cementitous systems, Cement Concr. Res. (2011).
[44] A. Kumar, Modelling hydration kinetics of cementitous systems, Doctoral Thesis, Ecole Polytechnique Federale de Lausanne, Switzerland 2012.
[45] P.W. Brown, The effect of inorganic salts on tricalcium silicate hydration, Cement Concr. Res. 16 (1985) 17–22.